

Radiation Assessment of a 56 Gbps Electro-Absorption Modulator Driver for Optical Intra-Satellite Links

Kieran De Bruyn , Arijit Karmakar , Warre Geeroms , Michael Vanhooeke , Laurens Bogaert , Günther Roelkens , Alan Naughton, David Mackey, Jeffrey Prinzie , Paul Leroux  and Johan Bauwelinck 

Abstract—This article presents a radiation-hardened-by-process 56 Gbps electro-absorption modulator driver designed in a 130 nm SiGe BiCMOS technology for application in optical intra-satellite links. Details of the driver architecture are provided, along with the electrical and optical measurement setups used to evaluate its performance. To assess the vulnerability of the driver against radiation exposure in the space environment, samples were irradiated with X-rays up to a total accumulated dose of 1.2 Mrad(Si), simulating the effects of Total Ionizing Dose (TID) in orbit. Furthermore, heavy-ion experiments corroborated the driver’s resilience to Single Event Transients (SETs) across a range of linear energy transfers (LETs) from 20 to 65.2 MeV cm²/mg, with a particle fluence of 1.2×10^7 cm⁻². No Single Event Latchup (SEL) was observed in the irradiated samples during the heavy-ion exposure.

Index Terms—Radiation hardening by process, radiation effects, optical transmitters, analog IC design

I. INTRODUCTION

TERRESTRIAL short reach optical communication links have consistently achieved speeds greater than 100 Gbps for quite some time now [1]–[3] due to continuous advancements in photonic devices, optical fiber technology, signal processing and modulation techniques. These technological advances, in addition to the growing demand for high-speed data transmission to support increased internet traffic and data center interconnects, have proven the feasibility and reliability of these links operating beyond 100 Gbps. An emerging trend in the satellite industry is to use these relatively mature terrestrial optical communications technologies in place of the bulky waveguide-based Radio Frequency (RF) interfaces that currently manage inter-satellite and intra-satellite communications links for e.g. onboard digital signal processors and

science instruments [4]. The adoption of optical interfaces, and more recently, the integration of photonic circuits, translates into significant reductions in terms of Size, Weight and Power (SWaP) of onboard equipment compared to conventional purely electrical RF transceivers, because the heavy metal waveguides can be replaced with lightweight optical fiber. This ultimately leads to cost-effective and power-efficient versatile satellite payloads.

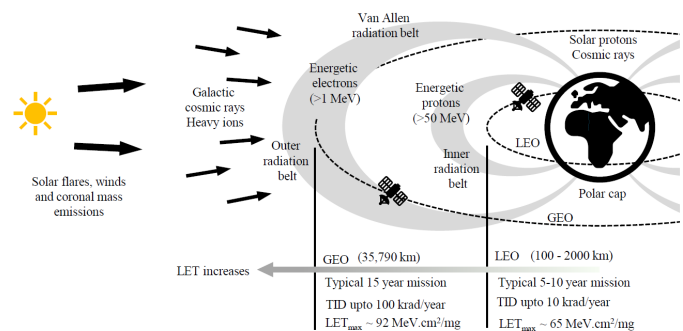


Fig. 1. The hazardous space-radiation environment around the Earth in space.

The severe space-radiation environment [5]–[8], illustrated in Fig. 1, presents a significant challenge for the reliable operation of electronic and optical communication interfaces on satellites and spacecraft. The activity of the Sun significantly modulates the terrestrial radiation environment around the Earth in space with short-term and long-term fluctuations along with the phase of the solar cycle. Beyond the Earth’s protective atmosphere, the principal amount of ionizing radiation in space originates from galactic cosmic rays (heavy ions and high-energy protons), solar flares and emissions (low-energy protons and magnetic flux), and the Van Allen radiation belt, which contain the trapped charged particles [9], [10]. Near geosynchronous orbits (GEO), the primary risk for satellites and spacecraft arises from heavy-ion-rich galactic cosmic rays and high-energy solar particles, which cause Single Event Effects (SEEs) like Single Event Upsets (SEUs) and Single Event Transients (SETs) in onboard components. The outer zone of the Van Allen radiation belt is dominated by energetic electrons, leading to Total Ionizing Dose (TID) and Displacement Damage (DD). Typically, TID levels can

Manuscript submitted July 18, 2024; revised October 10, 2024, December 12, 2024, January 21, 2025 and February 10, 2025; This work was supported in part by the ESA project ProtoBIX under Contract 4000130531/20/NL/AR, by MBRYONICS Ltd and by the Research Foundation Flanders (FWO) under grant 1SF3523N.

K. De Bruyn, A. Karmakar, W. Geeroms and J. Bauwelinck are with IDLab, Department of Information Technology, Ghent University-imec, Ghent, Belgium. (Corresponding author: K. De Bruyn, email:kieran.debruyne@ugent.be)

M. Vanhooeke was with IDLab, Ghent University-imec, Ghent, Belgium, now with NVIDIA, Ghent, Belgium

L. Bogaert and G. Roelkens are with Photonics Research Group, Ghent University-imec, Ghent, Belgium.

A. Naughton and D. Mackey are with MBRYONICS Ltd, Galway, Ireland. J. Prinzie and P. Leroux are with the Department of Electrical Engineering, KU Leuven, Geel, Belgium.

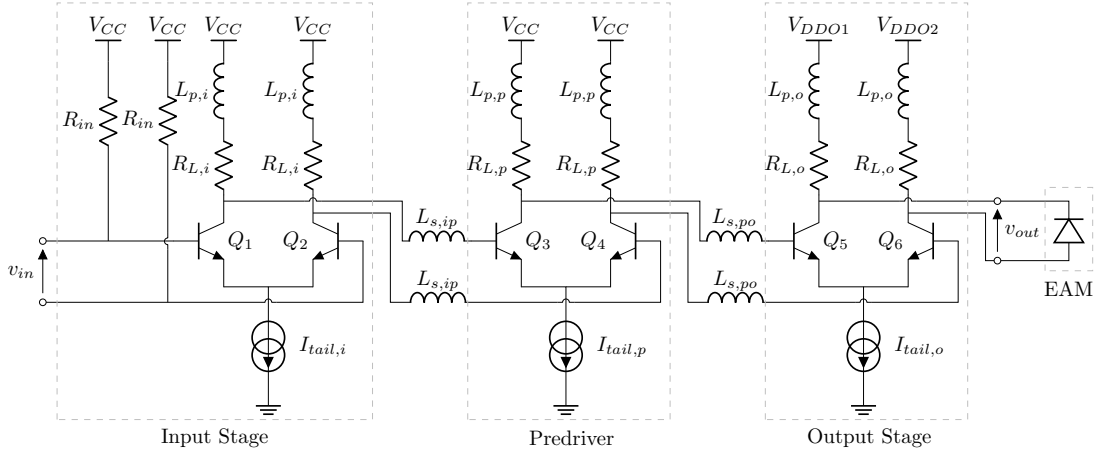


Fig. 2. Simplified schematic of a single channel of the proposed driver, ESD protection circuitry and corresponding matching networks omitted. The EAM will be implemented on a separate PIC. For the EAM to be biased correctly in the pictured orientation, $V_{DDO1} > V_{DDO2}$.

accumulate up to 100 krad/year in this region [11], necessitating multi-Mrad(Si) radiation-hardened satellite components. Although the impact of TID can be mitigated with an adequate shielding thickness, shielding is not effective in significantly reducing the impact of high-energy particles causing SEEs. The satellites in low Earth orbit (LEO) are primarily affected by high-energy trapped protons in the inner zone of the Van Allen radiation belt and there the TID levels can accumulate up to 10 krad/year [11]. For reliable operation, the LEO satellites necessitate a SEE and Single Event Latchup (SEL) tolerance up to Linear Energy Transfer (LET) of 60-65.2 MeV cm²/mg which extends to LET of 90-100 MeV cm²/mg for GEO satellites [12] and interplanetary space missions.

Currently, optical transceivers on satellites utilize optical technologies that are restricted to 12.5 Gbps per lane [12]–[14]. However, ongoing development efforts are targeted to achieve significantly higher line rates exceeding 25 Gbps or even 56 Gbps with newer high-speed radiation-hardened-by-process technologies such as silicon germanium (SiGe) or fully depleted silicon on insulator (FDSOI) [15]–[18]. Typically, as technology has scaled towards advanced nodes, the variations induced by TID tend to improve, while sensitivity to SEEs worsens [19], [20]. SiGe-based technologies are suitable for space applications considering their multi-Mrad(Si) immunity [15], however the SEEs are a concern in heavy-ion rich environments [21], [22]. Compared to electronic components, the optical or integrated photonic devices are experimentally found to be hardened up to multi-Mrad(Si) TID levels [23]–[26]. Recently, the propagation of SETs from the electrical domain to the photonic domain has been investigated, revealing potential impacts on data integrity in photonic interfaces. However, these occurrences can be mitigated by employing SEE-tolerant drivers [27].

The work presented in this paper focuses on the optical modulator driver for radiation hardened optical communication links. While radiation-hardened Vertical Cavity Surface Emitting Laser (VCSEL) drivers [28]–[32], Mach-Zehnder Modulator (MZM) drivers [33]–[36] and a Microring Modulator (MRM) driver [35] have been reported before, the targeted speed per channel of 56 Gbps is 1.4 times that of previously

reported radiation-hardened drivers. To the authors' knowledge, this makes this design the fastest radiation-hardened optical modulator driver reported thus far.

II. OPTICAL MODULATOR DRIVER DESIGN

The proposed optical transmitter comprises a silicon Photonic Integrated Circuit (PIC) with C-band SiGe Electro-Absorption Modulators (EAMs) and a SiGe BiCMOS driver IC which provides an appropriate bias and modulation voltage to the EAMs. EAM and MRM based transmitters generally consume significantly less power compared to MZMs [37], [38]. EAMs and MRMs induce a higher chirp to the optical carrier compared to MZMs, however, for intra-satellite links of a few meters long, the resulting dispersion is negligible [39], [40]. Both EAMs and MRMs provide sufficient bandwidth (> 50 GHz) [39], [40], but MRMs are more sensitive to temperature and wavelength variations and require accurate real-time wavelength locking which again increases the total power consumption of the transmitter [39], [40], so EAMs were selected as the appropriate modulator.

The EAM driver was implemented in a radiation assessed SiGe 130 nm BiCMOS process, whose Heterojunction Bipolar Transistors (HBTs) were found to withstand TIDs of 800 krad(Si) [41]. SiGe HBTs excel in high-speed analog and mixed-signal circuits, making them ideal for applications like the EAM driver, where high data rates are essential. Compared to CMOS, SiGe HBTs offer better speed, gain, and low noise at high frequencies, which are critical for telecom and datacom applications.

However, radiation hardening poses a challenge: techniques like enlarging transistors or using enclosed layouts increase parasitic capacitance, slowing circuit operation and limiting high-frequency performance. This trade-off becomes even more significant in radiation-sensitive environments like space, nuclear, terrestrial applications and high-energy physics experiments, where reliability must be prioritized over speed. Balancing these conflicting demands remains a key challenge in designing circuits that are both radiation-resistant and capable

of supporting high-speed communication. A more in depth discussion of these tradeoffs will follow at the end of this section.

A simplified schematic of the design can be found in Fig. 2, where Electrostatic Discharge (ESD) protection circuitry and the corresponding matching networks were omitted. The design consists of a cascade of three differential gain stages with shunt peaking inductors $L_{p,i}$, $L_{p,p}$ and $L_{p,o}$ [42]. The three stages are connected to each other with series peaking inductors $L_{s,ip}$ and $L_{s,po}$ to boost the electrical 3 dB-bandwidth of the driver. The output stage drives a Silicon Photonic (SiPh) EAM differentially, as in [43]. The two branches of the output stage receive a different supply voltage, V_{DDO1} and V_{DDO2} , to properly reverse bias the EAM.

The tail current sources are derived from a single current reference input using feedback-assisted current mirrors as shown in Fig. 3. This topology was chosen to obtain a low output compliance voltage to minimize the required supply voltage and thus limit the power consumption.

In addition to the inherent TID resistance of the SiGe HBTs, care was taken to further enhance radiation hardness, particularly against SEEs such as transients and latchups, which are harder to mitigate in high-speed designs. Including digital control circuitry on the high-speed ASIC adds potential points of failure due to radiation influence and should be avoided where possible. As such, digital equalization techniques or digital calibration blocks to compensate for variations are not present. Additionally, no switchable photocurrent sinking sources as in [43] are implemented. Instead, the output stage and its tail current source are designed to absorb the photocurrent expected from the SiPh EAM. This way, vulnerability to SEE-induced digital errors of the design is significantly reduced.

Additionally, to avoid latchup originating from radiation sources, neighboring NMOS and PMOS transistors in the current biasing circuitry are separated with double guard rings [44]. While this is a standard SEE mitigation technique, it was essential to further improve the radiation tolerance of the design, while keeping its high-speed performance acceptable.

As explored in [45], a reliable way to increase the radiation hardness of a Current Mode Logic (CML) SiGe-HBT design without sacrificing high speed performance is to increase the hardness of the DC current source. In the case of this design, this has been done by incorporating external negative feedback. To gauge the effect of SETs in this tail current source, some SPICE simulations were performed by modeling the SETs by the double-exponential current model of Eq. (1) [46], [47], where $I_{inject}(t)$ defines the current pulse caused by collecting a charge Q_{charge} . τ_f defines the fall time of the pulse, while τ_r defines the rise time. Both these parameters are heavily technology dependent. As such, in the simulation, these time constants are taken from a similar 130 nm CMOS technology [48] from the same vendor, specifically $\tau_r = 10$ ps and $\tau_f = 100$ ps.

$$I_{inject}(t) = \frac{Q_{charge}}{\tau_f - \tau_r} \left(e^{-\frac{t}{\tau_f}} - e^{-\frac{t}{\tau_r}} \right) \quad (1)$$

In this way, one critical point was identified. To achieve a sufficiently high output impedance in the feedback-assisted biasing current mirror, the current in the output branch of the opamp is fairly low. At the event of a strike of a charged particle

on this node, a current transient in the output branch will be generated. Because of the low current in this branch, this node is extra sensitive to this disruption, which will affect the gate voltage of M_3 . To simulate this effect, double exponential current transients with an equivalent charge of 1 pC and 10 pC are injected into the output node of the opamp. According to [48], [49], this approximately matches a LET of 1 to 10 MeV cm²/mg and 10 to 100 MeV cm²/mg respectively, depending on the exact collection depth. During the simulation, the node voltage and the output of the driver are monitored. The result can be seen in Fig. 4a, where it is clear that after 5 ns, there is still a considerable voltage difference at the output node of the opamp. This will thus affect the emitter voltage of the HBTs. In the branch of the differential pair with the lower supply voltage, the collector-emitter voltage V_{CE} of the HBT is already limited compared to the branch with the higher supply voltage. The decreased V_{CE} resulting from the additional voltage at the output of the opamp of the current source will thus make that transistor move closer to the saturation region. The more this effect takes place, the more the f_T of the transistor will decrease [50], which corresponds to a slower rise time. This can be seen in Fig. 4b and is further confirmed by the fact that the slower transitions move from the rising edges to the falling edges when V_{DDO1} and V_{DDO2} are switched.

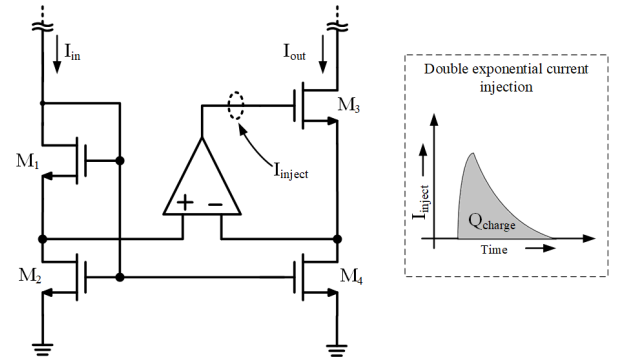


Fig. 3. The biasing tail current mirror circuit with the sensitive node used for SET simulation using a double exponential current with injected charge Q_{charge} .

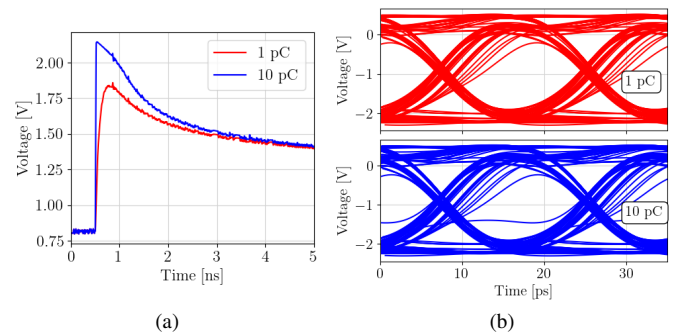


Fig. 4. SET simulations of critical node for injected charge of 1 pC (red) and 10 pC (blue). (a) Node voltage (b) Eye Diagram at output of the driver captured during the same 5 ns interval.

To conclude this section, the tradespace of a general radiation hardened optical driver Integrated Circuit (IC) is explored.

The main parameter that is determined by the designer of such a circuit is the current throughout the output stage. Increasing this parameter will have a fourfold effect: The driving voltage, determined in its simplest approximation by the internal termination resistor and Ohm's law, will increase. Naturally the total power consumption of the driver will increase as well. Thirdly, the bandwidth of the driver will reduce, as there is an optimal current associated to maximal f_T of the HBTs. Finally, since the total current in the branches is higher, the deviation by any current induced by a particle strike will have relatively lower impact.

There are some other parameters that change when irradiating, the most impactful of which being the current gain of the HBT. However, since any good design using HBTs is robust against variations in current gain, this radiation induced effect is inherently negated. In the case of this work, since the collector current in the output stage is fixed, a change in current gain β of the HBTs means a change in base current. By making sure that the main current in the previous stage is large enough compared to the base current, no noticeable change occurs in base bias voltage. For signal voltages, the fact that the output load of the previous stage is small compared to the input impedance of the transistors means that there is only a voltage signal transfer, the transfer of a current signal is too small to be considered. Other parameters like transit time, f_T and f_{max} also degrade, but those values change only negligibly for the radiation levels considered in this work [51].

A final choice in the hands of a designer is the type of transistor with which to build the circuit. Other choices than the npn HBTs used in this work could be pnp HBTs [22] or SiGe HBTs used in inverse-mode [52], which have shown to be more robust to TID effects and to have an improved SET response, respectively. However, both alternative choices are associated with lower achievable speeds, which is why they were not considered in this work.

III. ELECTRICAL AND OPTICAL MEASUREMENTS

A micrograph of the fabricated die can be seen in Fig. 5. Initially, the electrical properties of the unirradiated driver were measured. The frequency response was measured by connecting a Vector Network Analyzer (VNA) using RF probes to the sample as in Fig. 6a. As shown in Fig. 7, for an input power of -5 dBm, the electrical 3 dB-bandwidth was determined to be 39 GHz. The increasing bandwidth for high input powers is explained by the fact that the driver is only able to deliver a certain peak-peak output voltage, which is mostly limited by supply voltage and tail current. The gain predicted by a small-signal analysis (which corresponds the low input power case) would put the output voltage over that limit when a large enough input voltage is applied. This will make the gain at lower frequencies effectively compress, which looks like the bandwidth expanding.

The time domain performance of the driver was tested by the setup of Fig. 6b. A 92 GSa/s Arbitrary Waveform Generator (AWG) was used to generate a 300 mVppd, 56 GBd Non-Return-to-Zero (NRZ) Pseudo-Random Bit Sequence (PRBS)-13 signal. The driver was connected by RF probes. The

TABLE I
ELECTRICAL MEASUREMENTS

Specification	Value
Large signal electrical bandwidth	39 GHz
Differential output swing	1.5 Vppd
Output bias range	-1.5 to 1.5 V
Power consumption (4 channels)	250 mW
Power efficiency at 56 Gbps	1.1 pJ/b

output signal was then measured using a 256 GSa/s sampling oscilloscope. The eye diagram of this measurement can be seen in Fig. 8a.

However, the load presented by the oscilloscope is 50Ω on each measurement channel, while an EAM presents a purely capacitive load. Since the internal load resistors, $R_{L,o}$ in Fig. 2, are also 50Ω . The output impedance thus effectively becomes 25Ω . This will cause the output swing to double for the EAM compared to the electrical measurements on the scope, since it is set by the current through the output impedance. The electrical measurements are summarized in Table I

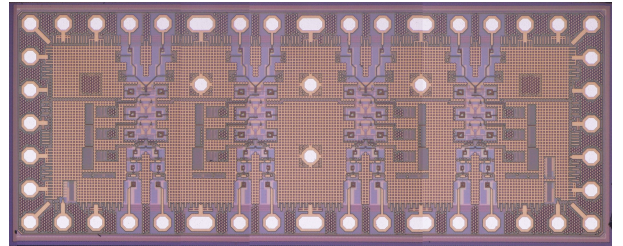


Fig. 5. Micrograph of the proposed driver chip ($2720 \mu\text{m} \times 1070 \mu\text{m}$).

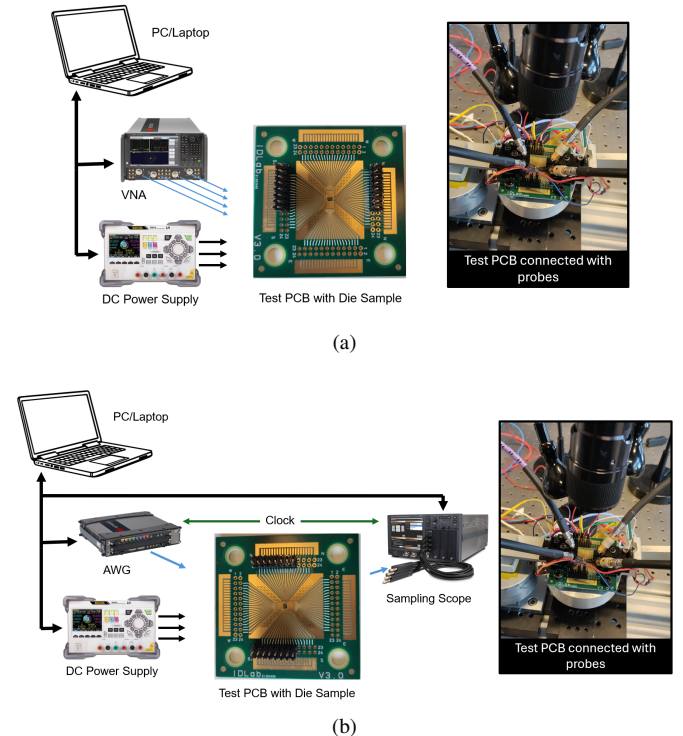


Fig. 6. Measurement setups for the (a) VNA measurement (b) electrical time domain measurement

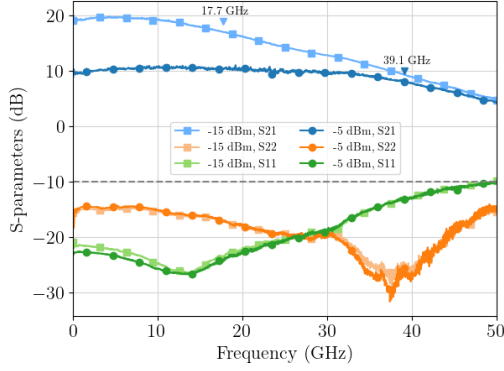


Fig. 7. Measured S-parameters. S_{dd21} in blue, S_{dd11} in orange, S_{dd22} in green. Circle markers for input power of -15 dBm, square markers for input power of -5 dBm. 3-dB bandwidth annotated.

To analyze the unirradiated optical performance of the driver, it was put in a relatively simple optical test setup, as shown in Fig. 9. The driver IC and the PIC containing the EAM were mounted on a PCB and wirebonded to each other as shown in Fig. 9a. The co-designed PIC was fabricated on imec’s iSiPP50G SiPh platform. A Continuous Wave (CW) laser was coupled into a polarisation controller and then into the PIC using a fiber array mounted on a dedicated alignment system. The same NRZ PRBS-13 input signal was supplied using a 92 GSa/s AWG connected with a TR-70 connector and PCB traces wire-bonded to the input bondpads of the driver. The AWG output signal was pre-compensated for the frequency dependent losses in the cables and TR-70 connector. Since no dedicated Transimpedance Amplifier (TIA) was used, the optical output signal was amplified using a benchtop Erbium Doped Fiber Amplifier (EDFA) before a 70 GHz reference photodiode connected to a 256 GSa/s sampling oscilloscope.

The driver is able to provide a 1.5 Vppd, 56 Gbps signal to the EAM, which is biased near the point of optimal Extinction Ratio (ER) versus Insertion Loss (IL) tradeoff, or 1.3 V reverse bias ($V_{DDO1} = 2$ V and $V_{DDO2} = 3.3$ V) at a laser wavelength of 1530 nm. The resulting eye diagram measured at the output of the photodiode can be seen in Fig. 8b. The ER reached was 2.4 dB and could be improved to 2.8 dB by increasing the bias voltage over the EAM to 1.5 V by increasing the greater of V_{DDO1} and V_{DDO2} to 3.5 V, and slightly increasing the supply voltage from 1.2 V to 1.3 V. This will evidently also increase the power consumption of the driver. However, a higher bit rate signal can now be transmitted, as shown in Fig. 8c. The resulting power efficiency without accounting for the laser power is now 0.9 pJ/b.

IV. RADIATION CHARACTERIZATION

A. Total Ionizing Dose (TID)

The TID test was performed at KU Leuven, Geel campus, Belgium, using an X-ray source, with a spot size diameter of approximately 3 cm. The test setup is visible in Fig. 10a. The X-ray beam is generated from a 23 keV, 15 mA W-tube. Prior to exposure of the sample to radiation, the X-ray beam’s dose

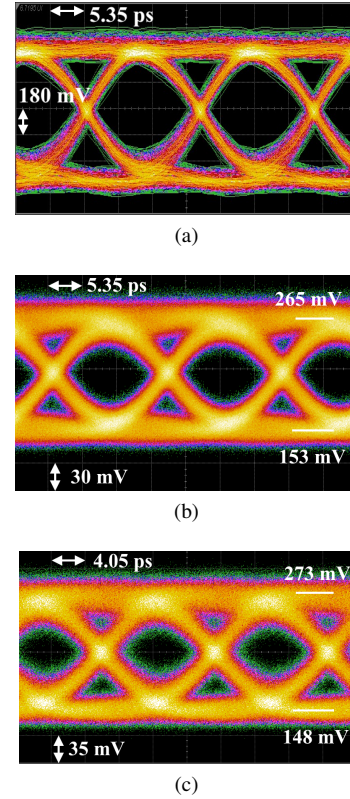


Fig. 8. (a) Electrical eye diagram for 56 Gbps PRBS-13 NRZ (b) Electro-optical eye diagram for 56 Gbps PRBS-13 NRZ (c) Electro-optical eye diagram for 74 Gbps PRBS-13 NRZ with increased bias and supply voltage.

rate was calibrated using a PIN diode-based radiation detector. In order to emulate the Low Earth Orbit (LEO) environment, multiple samples were exposed to a dose rate of 25 krad(Si)/h, for a total dose of 1.2 Mrad(Si). [53]. Since Enhanced Low Dose Rate Sensitivity (ELDRS) is not present in SiGe-based HBTs [15], a slightly higher dose rate was chosen to cover a longer lifetime (> 5 years) of the satellite with the test.

All devices were irradiated at room temperature while connected to the appropriate supplies. After irradiation, half of the samples were annealed for 24 h at ambient temperature, the other half were put in a temperature controlled chamber for 7 days at 100 °C. Each annealing technique was tested with four samples, which means that in total eight samples were tested.

The frequency response was measured with a Keysight P5028A vector network analyzer before and after irradiation, as well as during irradiation for the devices connected to supply. The RF level applied to the inputs of the driver for this test is -5 dBm. The result is shown in Fig. 11, where it is clear that at 1.2 Mrad(Si) irradiation, there is only 0.1 dB difference in frequency response compared to the pre-irradiation measurement results. The measurements pre- and post-irradiation were conducted on the entire package, including a TR70 connector and dedicated PCB. There is thus a difference in achieved bandwidth of a few GHz compared to the results discussed in Fig. 7.

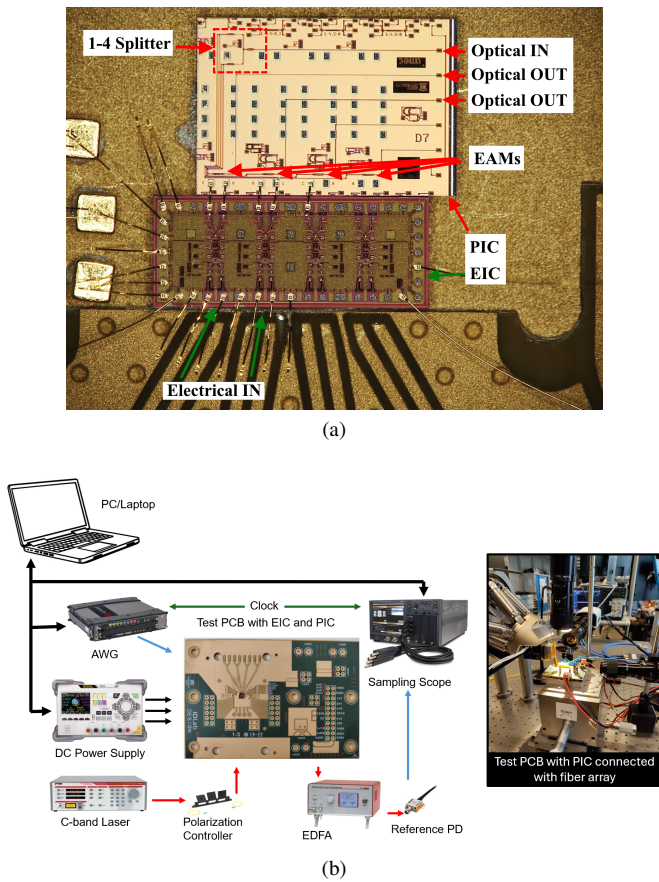


Fig. 9. Measurement setups for the optical time domain measurements (a) closeup of wirebonded driver and PIC (b) overview

B. Single Event Effects (SEEs)

The SEE tests were performed at the cyclotron of Catholique Université de Louvain, Louvain-la-Neuve, Belgium. The heavy-ion test setup can be seen in Fig. 10b. The cyclotron had accelerated heavy ions in a range of LETs from 20.4 to 65.2 MeV cm²/mg (⁵⁸Ni¹⁸⁺, ⁸⁴Kr²⁵⁺, ¹⁰³Rh³¹⁺, ¹²⁴Xe³⁵⁺). The ion energies were 582 MeV, 769 MeV, 957 MeV and 995 MeV respectively. The chip was mounted inside the radiation chamber, under vacuum and at ambient temperature, and the input was connected using SMA cables to a signal generator, which generates a sine wave of the appropriate input level with a frequency ranging from 10 to 1000 MHz. Although this is much lower than the bandwidth of the fabricated driver, the upper limit of this frequency range is caused by the minimal pulse width the Real-Time Oscilloscope (RTO) can trigger on. The output was connected to a Keysight DSAZ634A RTO, which was configured to trigger on pulses less wide than half the input sine wave period. The trigger output of the RTO was then connected to a universal counter, which thus counts the number of times that SET pulses cross the mid-level, and thus could, at full rate, introduce bit errors. During the test, each sample was irradiated with a flux of 1.5×10^4 particles/s/cm² until a fluence of 1.2×10^7 particles/cm² was reached.

A snapshot of the SET with the longest pulse duration (5 ns) observed during the measurement can be seen in Fig. 12. The amount of SETs counted for different input frequencies and

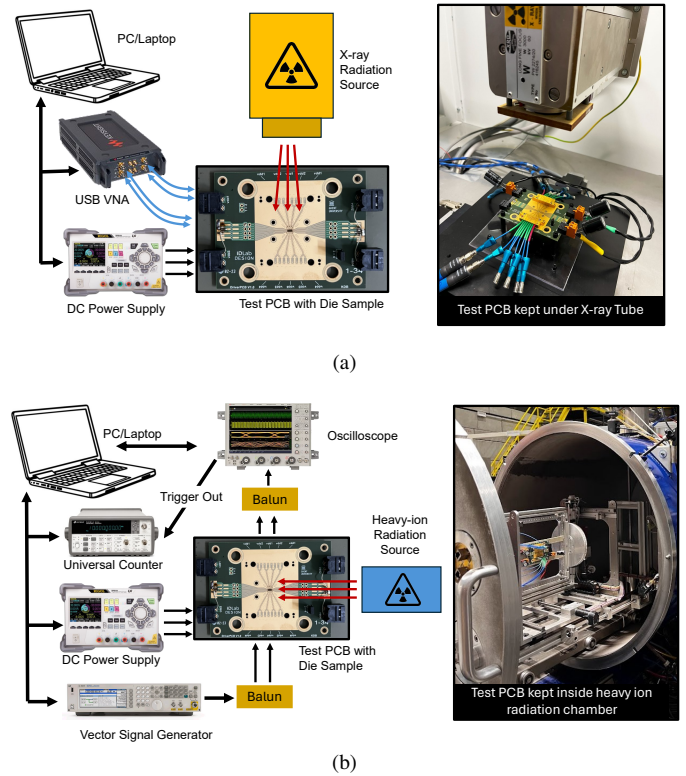


Fig. 10. Measurement setups for the (a) TID measurement (b) SEE measurement

LET can be seen in Fig. 13. To fit a Weibull distribution (Eq. (2)) to the data points, all measurements where no SETs were observed are ignored, although they were taken into account when calculating the confidence interval as in [54]. The onset is chosen at the highest energy where zero SETs were observed, and the rest of the parameters are fitted using a non-linear least squares method to the worst-case measurements for each LET. The fitted parameters are summarised in Table II.

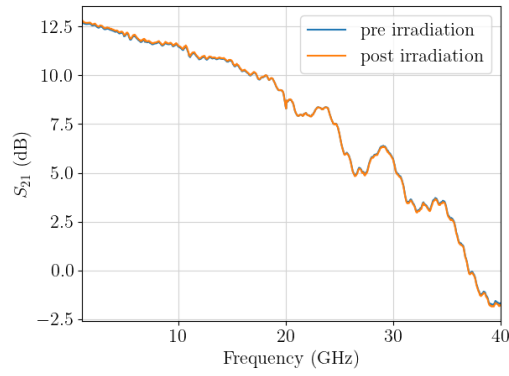
$$\sigma = \sigma_{sat} \left(1 - e^{-\left(\frac{LET - Onset}{W}\right)^s} \right) \quad (2)$$

To obtain a lower bound for the Mean Time Between Events (MTBE), the integral flux at the onset LET, as measured in [55], assuming LEO orbit, is multiplied by the saturation cross-section.

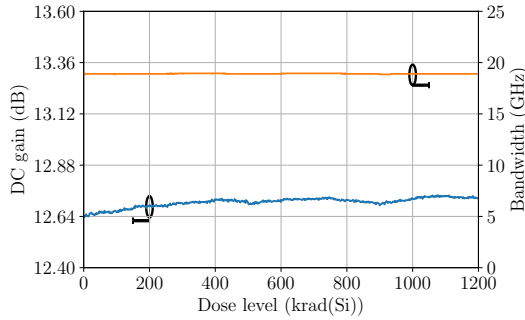
TABLE II
WEIBULL PARAMETERS IN FIG. 13 AND MTBE CALCULATION

Parameter	10 MHz fit	100 MHz fit
σ_{sat} [cm ²]	2.39×10^{-6}	8.88×10^{-7}
Onset [MeV cm ² /mg]	20.4	16.1
W [MeV cm ² /mg]	60.9	44.7
s [-]	1	2
Integral flux at onset LET [55][particles/cm ² /day]	8×10^{-3}	1×10^{-2}
MTBE [years]	143000	309000
Estimated Bit Error Rate (BER) [35] at 56 Gbps [-]	6.4×10^{-13}	2.4×10^{-13}

To monitor SEL, the power supply used to bias the samples was recorded, to check whether the current limit of twice the nominal current was reached. No latchup was observed during this experiment.



(a)



(b)

Fig. 11. (a) Frequency response of the driver including PCB traces and TR-70 connector before and after 1.2 Mrad(Si) irradiation. (b) Evolution of DC gain and bandwidth with dose level.

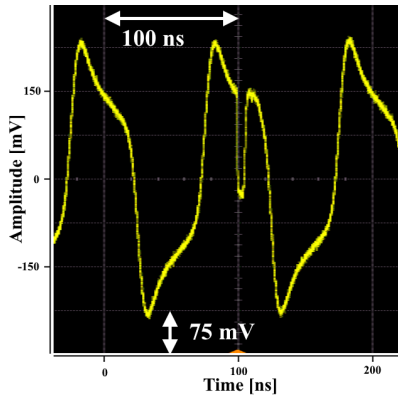


Fig. 12. Closeup of SET event with a 10 MHz input signal.

V. DISCUSSION

The driver chips were irradiated with X-ray to assess their performance degradation at a TID level of 1.2 Mrad(Si). As shown in Fig. 11, the bandwidth remained consistent throughout the experiment, while the gain exhibited minor variations. Interestingly, a subtle gain increase was observed with increasing TID. This can be attributed to the decrease in the threshold voltage of the n-channel MOSFETs used inside the current mirror circuit to bias the drivers. After irradiation, the samples were subjected to annealing, and no major variations were observed during the process.

The samples were also tested with heavy-ions at different LET

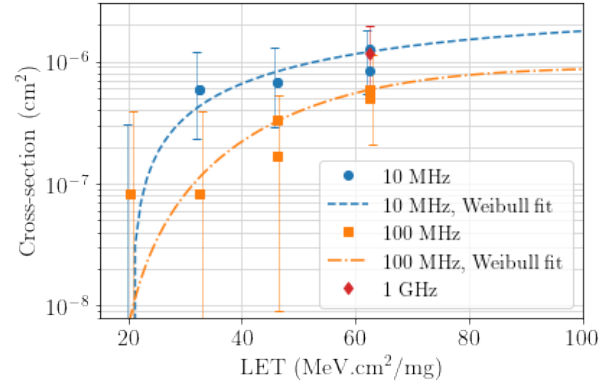


Fig. 13. SET Cross-section after a fluence of 1.2×10^7 particles/cm² has been reached. The error bars are defined by the 95 %-confidence interval, as in [54]. Lower bound of confidence interval for 20.4 and 32.4 MeV cm²/mg at 100 MHz is 4×10^{-11} cm², for 20.4 MeV cm²/mg at 10 MHz it is 0 cm².

TABLE III
STATE-OF-THE-ART COMPARISON OF RADIATION-TESTED ELECTRO-OPTICAL TRANSMITTERS FOR SPACE APPLICATIONS.

	[30]	[36]	[31]	[32]	This work
Channels	1	1	12	4	4
Targeted device	VCSEL	MZM	VCSEL	VCSEL	SiPh EAM
Bit rate (Gbps)	6.25	10	28	40	56
Extinction Ratio (dB)	-	2.5	5	-	2
Power (mW/ch)	210	115 [†]	314 [*]	100	62.5 [†]
Energy Efficiency(pJ/b)	33.6	11.5 [†]	11.2 [*]	2.5	1.1 [†]
TID tolerance (krad(Si)) [§]	100	1×10^6	107	100	1200
LET _{max} (MeV cm ² /mg) [§]	62	-	66.7	-	65.2
Saturated cross-section (cm ²)	4.8×10^{-4}	-	3.6×10^{-3}	-	2.4×10^{-6}

* Combined power (TX+RX), [†]Laser power not included. [§]Highest tested

values. Starting from 20 MeV cm²/mg, SETs with variable pulse duration were observed, ranging from 0.1 to 5 ns, invariable with LET. In the worst case, at the full-rate of 56 Gbps, this pulse could introduce a 280-bit long burst error. This worst case scenario is probably related to the critical node identified in Fig. 4, although further experiments should be done to verify that claim. One possible solution to this problem could be increasing the collector current, such that the driver would be more robust to the increased rise time caused by the change in V_{CE} , as discussed in Section II. However, this would likely require a vast increase in current, which would cause the impressive 1.1 pJ/b energy efficiency to plummet. During the experiment, the maximum number of SETs, 15, was observed with an LET of 65.2 MeV cm²/mg. However, the calculated lower bound for the MTBE is more than 143000 years, which means that it is unlikely that an SET will be observed during the lifetime of the satellites.

The estimated bit-error-rate (BER) (as per [35]) values at 56 Gbps using the optical modulator corresponding to cross-section of 2.39×10^{-6} cm² and 8.88×10^{-7} cm², are 6.4×10^{-13} and 2.4×10^{-13} respectively. SELs were not observed during the experiment, which establishes the driver's immunity against latch-up events for ion energies less than 65.2 MeV cm²/mg in vacuum at ambient temperature.

A state-of-the-art comparison of reported electro-optical transmitters for space applications is made in Table III. The VCSEL driver in [30] was implemented in a 130 nm SiGe

process and targeted 6.25 Gbps communication links in satellites. The drivers had been qualified with the space-radiation standards, but at the expense of very high power consumption. Compared to [30], the optical driver as reported in [36] achieved higher bit rate (10 Gbps) and tested up to a TID level of 1 Grad(Si), while being more power efficient than [30]. A radiation-hardened optical transceiver modules with 12 parallel channels, achieving 28 Gbps bit rate per channel were reported in [31]. The 4-channel optical driver of [32] achieved 40 Gbps bit rate per channel. The drivers in [36] and [32] have not been tested with heavy-ions, but [32] underwent SEE radiation testing with maximum proton energy levels of 60 MeV. No data related to effective LET values were reported in [36] and [32]. In comparison, this work's optical modulator achieves 1.4 times the bit rate per channel (56 Gbps) with an energy efficiency of 1.1 pJ/b. Even if the laser power is to be taken into account, which is estimated to be an extra 0.5 pJ/b, energy efficiency is still the best among Table III. To the author's knowledge, this work showcases the best energy efficiency, bit rate, and radiation tolerance in comparison to its counterparts [30]–[32], [36] designed for space applications.

VI. CONCLUSION

This radiation assessment study presents the development and the performance evaluation of a high-speed, radiation-tolerant modulator driver designed for 56 Gbps electro-absorption modulator applications in intra-satellite optical links. The driver is designed in a radiation-hardened-by-process 130 nm SiGe BiCMOS process and is shown to drive an EAM at speeds up to 74 Gbps with a power efficiency of 0.9 pJ/b. To assess its performance in a realistic space environment, the driver underwent a comprehensive radiation hardness evaluation. This assessment included X-ray irradiation up to the TID level of 1.2 Mrad(Si) and heavy-ion exposure to evaluate SEE susceptibility across a range of LETs from 20 to 65.2 MeV cm²/mg with a fluence of 1.2×10^7 cm⁻². The TID experiments resulted in a maximum 0.1 dB deviation in the driver's frequency response after 1.2 Mrad(Si) of irradiation, and after a fluence of 1.2×10^7 cm⁻² of ions with a LET of 65.2 MeV cm²/mg, only 15 SETs were observed. The driver's functionality remained uninhibited throughout these experiments, and no SEL event was observed, showcasing its significant radiation tolerance. These conclusions validate the suitability of this driver design for future high-bandwidth, reliable intra-satellite optical communication for critical space applications.

ACKNOWLEDGMENT

The authors would like to thank IHP for providing access to the SG13RH process and Keysight Technologies for lending a 40GHz P5028A VNA.

REFERENCES

- [1] T. Fujisawa *et al.*, "4×25-Gbit/s, 40-km SMF transmission based on 1.3- μ m electroabsorption modulators integrated with DFB lasers for 100-Gbit/s ethernet," in *Opto-Electronics and Communications Conference (OECC) 2010 Technical Digest*, Jul. 2010, pp. 50–51.
- [2] T. Ohyama *et al.*, "Compact hybrid-integrated 100-Gbit/s TOSA for 40-km transmission," in *2015 Opto-Electronics and Communications Conference (OECC)*, Dec. 2015, pp. 60–62.
- [3] S. Niu *et al.*, "A Linear Modulator Driver With Over 70-GHz Bandwidth 21.8-dB Gain and 3.4-Vppd Output Swing for Beyond 120-GbD Optical Links," *IEEE Trans. Microw. Theory Tech.*, vol. 72, no. 7, pp. 4080–4091, Dec. 2024.
- [4] K. Balakier *et al.*, "Photonic integrated circuit technology for communication satellites payloads," in *49th European Conference on Optical Communications (ECOC 2023)*, vol. 2023, Oct. 2023, pp. 1627–1631.
- [5] A. Vampola, "The hazardous space particle environment," *IEEE Trans. Plasma Sci.*, vol. 28, no. 6, pp. 1831–1839, Dec. 2000.
- [6] S. Bourdarie *et al.*, "The Near-Earth Space Radiation Environment," *IEEE Trans. Nucl. Sci.*, vol. 55, no. 4, pp. 1810–1832, Aug. 2008.
- [7] M. A. Xapsos *et al.*, "Near-Earth Space Radiation Models," *IEEE Trans. Nucl. Sci.*, vol. 60, no. 3, pp. 1691–1705, Jun. 2013.
- [8] J. Barth *et al.*, "Space, atmospheric, and terrestrial radiation environments," *IEEE Trans. Nucl. Sci.*, vol. 50, no. 3, pp. 466–482, Jun. 2003.
- [9] A. Karmakar *et al.*, "A Review of Semiconductor Based Ionising Radiation Sensors Used in Harsh Radiation Environments and Their Applications," *Radiation*, vol. 1, no. 3, pp. 194–217, Aug. 2021.
- [10] I. Jun *et al.*, "A review on radiation environment pathways to impacts: Radiation effects, relevant empirical environment models, and future needs," *Advances in Space Research*, Apr. 2024, in press.
- [11] M. A. Xapsos, "Modeling the Space Radiation Environment," in *2006 IEEE Nuclear and Space Radiation Effects Conference (NSREC), Short Course*, Jul. 2006.
- [12] S. Giannakopoulos *et al.*, "A 112 Gb/s radiation-hardened mid-board optical transceiver in 130-nm SiGe BiCMOS for intra-satellite links," *Frontiers in Physics*, vol. 9, art. no. 672941, May 2021.
- [13] J. Lauzon *et al.*, "Reliability of connectorized 10gbps/channel optical fiber transceivers," in *2016 IEEE Avionics and Vehicle Fiber-Optics and Photonics Conference (AVFOP)*, Nov. 2016, pp. 277–278.
- [14] R. T. Logan *et al.*, "Radiation Test Results for Glenair 5 Gbps and 40 Gbps (4x10 Gbps) Optical Transceivers," in *2019 IEEE Radiation Effects Data Workshop*, Jul. 2019, pp. 101–108.
- [15] J. D. Cressler, "Radiation Effects in SiGe Technology," *IEEE Trans. Nucl. Sci.*, vol. 60, no. 3, pp. 1992–2014, Jun. 2013.
- [16] J. Solano *et al.*, "Total Ionizing Dose Response of Commercial 22nm FD-SOI CMOS Technology," in *2022 IEEE Radiation Effects Data Workshop (REDW) (in conjunction with 2022 NSREC)*, Jul. 2022, pp. 100–104.
- [17] Y. Yin *et al.*, "Total ionizing dose and single event effect response of 22 nm ultra-thin body and buried oxide fully depleted silicon-on-insulator technology," *Microelectronics Reliability*, vol. 152, art. no. 115296, Jan. 2024.
- [18] G. Termo *et al.*, "Characteristics and ultra-high total ionizing dose response of 22 nm fully depleted silicon-on-insulator," *Journal of Instrumentation*, vol. 19, no. 03, art. no. C03039, Mar. 2024.
- [19] D. M. Fleetwood, "Evolution of total ionizing dose effects in MOS devices with Moore's law scaling," *IEEE Trans. Nucl. Sci.*, vol. 65, no. 8, pp. 1465–1481, Aug. 2018.
- [20] D. Kobayashi, "Scaling Trends of Digital Single-Event Effects: A Survey of SEU and SET Parameters and Comparison With Transistor Performance," *IEEE Trans. Nucl. Sci.*, vol. 68, no. 2, pp. 124–148, Feb. 2021.
- [21] N. E. Lourenco *et al.*, "The impact of technology scaling on the single-event transient response of SiGe HBTs," *IEEE Trans. Nucl. Sci.*, vol. 64, no. 1, pp. 406–414, Jan. 2017.
- [22] A. Ildefonso *et al.*, "Tradeoffs Between RF Performance and SET Robustness in Low-Noise Amplifiers in a Complementary SiGe BiCMOS Platform," *IEEE Trans. Nucl. Sci.*, vol. 67, no. 7, pp. 1521–1529, Jul. 2020.
- [23] S. S. El Nasr-Storey *et al.*, "Effect of radiation on a Mach-Zehnder interferometer silicon modulator for HL-LHC data transmission applications," *IEEE Trans. Nucl. Sci.*, vol. 62, no. 1, pp. 329–335, Feb. 2015.
- [24] M. Zeiler *et al.*, "Radiation damage in silicon photonic Mach-Zehnder modulators and photodiodes," *IEEE Trans. Nucl. Sci.*, vol. 64, no. 11, pp. 2794–2801, Nov. 2017.
- [25] P. S. Goley *et al.*, "Total ionizing dose effects in 70-GHz bandwidth photodiodes in a SiGe integrated photonics platform," *IEEE Trans. Nucl. Sci.*, vol. 66, no. 1, pp. 125–133, Jan. 2019.
- [26] S. Cammarata *et al.*, "Compact silicon photonic Mach-Zehnder modulators for high-energy physics," *Journal of Instrumentation*, vol. 19, no. 03, art. no. C03009, Mar. 2024.
- [27] G. N. Tzintzarov *et al.*, "Electronic-to-Photonic Single-Event Transient Propagation in a Segmented Mach-Zehnder Modulator in a Si/SiGe Integrated Photonics Platform," *IEEE Trans. Nucl. Sci.*, vol. 67, no. 1, pp. 260–267, Jan. 2020.

- [28] P. Leroux *et al.*, "Design and Assessment of a Circuit and Layout Level Radiation Hardened CMOS VCSEL Driver," *IEEE Trans. Nucl. Sci.*, vol. 54, no. 4, pp. 1055–1060, Sep. 2007.
- [29] G. Mazza *et al.*, "High-Speed, Radiation-Tolerant Laser Drivers in 0.13 μm CMOS Technology for HEP Applications," *IEEE Trans. Nucl. Sci.*, vol. 61, no. 6, pp. 3653–3659, Dec. 2014.
- [30] A. Tanskanen *et al.*, "Radiation Tolerant 6.25 Gbps 850nm Optical Transceiver," in *2017 17th European Conference on Radiation and Its Effects on Components and Systems (RADECS)*, Oct. 2017, pp. 532–535.
- [31] N. Safdari *et al.*, "Reliability Testing of 28Gbps/channel Fiber Optics Transceivers for Space Applications," in *2022 International SpaceWire & SpaceFibre Conference (ISC)*, Oct. 2022, pp. 113–120.
- [32] I. Sourikopoulos *et al.*, "A 40Gb/s Rad-Hard Quad VCSEL Driver Integrated Circuit in 130nm SiGe BiCMOS for Intra-Satellite Optical Interconnects," in *2024 15th International Conference on Space Optics (ICSO)*, Oct. 2024, forthcoming.
- [33] S. Cammarata *et al.*, "Design and Performance Evaluation of Multi-Gb/s Silicon Photonics Transmitters for High Energy Physics," *Energies*, vol. 13, no. 14, art. no. 3569, Jul. 2020.
- [34] G. Ciarpi *et al.*, "Design of radiation-hard MZM drivers," in *20th Italian National Conference on Photonic Technologies (Fotonica 2018)*, May 2018, pp. 100–104.
- [35] G. Ciarpi *et al.*, "Design, Implementation, and Experimental Verification of 5 Gbps, 800 Mrad TID and SEU-Tolerant Optical Modulators Drivers," *IEEE Trans. Circuits Syst. I*, vol. 67, no. 3, pp. 829–838, Mar. 2020.
- [36] G. Ciarpi *et al.*, "Design and Characterization of 10 Gb/s and 1 Grad TID-Tolerant Optical Modulator Driver," *IEEE Trans. Circuits Syst. I*, vol. 69, no. 8, pp. 3177–3189, Aug. 2022.
- [37] S. S. Azadeh *et al.*, "Low V_{π} Silicon photonics modulators with highly linear epitaxially grown phase shifters," *Opt. Express*, vol. 23, no. 18, pp. 23 526–23 550, Sep. 2015.
- [38] J. Witzens, "High-speed silicon photonics modulators," *Proceedings of the IEEE*, vol. 106, no. 12, pp. 2158–2182, Dec. 2018.
- [39] G. Ghione, *Semiconductor Devices for High-Speed Optoelectronics*. Cambridge University Press, 2009.
- [40] M. Pantouvaki *et al.*, "Active Components for 50 Gb/s NRZ-OOK Optical Interconnects in a Silicon Photonics Platform," *Journal of Lightwave Technology*, vol. 35, no. 4, pp. 631–638, Feb. 2017.
- [41] M. Krstic *et al.*, "Evaluierung einer strahlungsharten Bibliothek in 0.13 μm BiCMOS," in *DLR Bauteilekonferenz*. Ulm, Germany, Apr. 2018.
- [42] E. Säckinger, *Broadband Circuits for Optical Fiber Communication*. Wiley & sons Ltd., 2005.
- [43] H. Ramon *et al.*, "70 Gb/s low-power DC-coupled NRZ differential electro absorption modulator driver in 55 nm SiGe BiCMOS," *J. Lightw. Technol.*, vol. 37, no. 5, pp. 1504–1514, Feb. 2019.
- [44] S. J. Gaul *et al.*, *Integrated Circuit Design for Radiation Environments*. Wiley & Sons Ltd., 2019.
- [45] M. A. R. Sarker *et al.*, "Mitigation of single-event effects in sige-hbt current-mode logic circuits," *Sensors*, vol. 20, no. 9, art. no. 2581, May 2020.
- [46] G. C. Messenger, "Collection of charge on junction nodes from ion tracks," *IEEE Trans. Nucl. Sci.*, vol. 29, no. 6, pp. 2024–2031, Dec. 1982.
- [47] D. Monda *et al.*, "Analysis and Comparison of Rad-Hard Ring and LC-Tank Controlled Oscillators in 65 nm for SpaceFibre Applications," *Sensors*, vol. 20, no. 16, art. no. 4612, Aug. 2020.
- [48] M. Andjelkovic *et al.*, "Comparison of the SET sensitivity of standard logic gates designed in 130 nm CMOS technology," in *2017 IEEE 30th International Conference on Microelectronics (MIEL)*, Oct. 2017, pp. 217–220.
- [49] L. Massengill *et al.*, "SEU error rates in advanced digital CMOS," in *RADECS 93. Second European Conference on Radiation and its Effects on Components and Systems (Cat. No.93TH0616-3)*, Sep. 1993, pp. 546–553.
- [50] C. T. Kirk, "A theory of transistor cutoff frequency (fT) falloff at high current densities," *IRE Transactions on Electron Devices*, vol. 9, no. 2, pp. 164–174, Mar. 1962.
- [51] J. D. Cressler *et al.*, *Silicon-Germanium Heterojunction Bipolar Transistors*. Artech House Inc., 2002.
- [52] Z. E. Fleetwood *et al.*, "SiGe HBT Profiles With Enhanced Inverse-Mode Operation and Their Impact on Single-Event Transients," *IEEE Trans. Nucl. Sci.*, vol. 65, no. 1, pp. 399–406, Jan. 2018.
- [53] O. Gutiérrez *et al.*, "Toward the Use of Electronic Commercial Off-the-Shelf Devices in Space: Assessment of the True Radiation Environment in Low Earth Orbit (LEO)," *Electronics*, vol. 12, no. 19, art. no. 4058, Sep. 2023.
- [54] *Single Event Effects Test Method and Guidelines, ESCC Basic Specification No. 25100*, European Space Components Coordination (ESCC), Jun. 2014, Issue 2 Draft A.
- [55] X. Liang *et al.*, "Impact of heavy-ion irradiation on gate oxide reliability of silicon carbide power MOSFET," *Radiation Effects and Defects in Solids*, vol. 176, pp. 1038–1048, Nov. 2021.